Marew *et al. Earth, Planets and Space* (2025) 77:31
https://doi.org/10.1186/s40623-025-02147-3

Earth, Planets and Space

FULL PAPER **Open Access**

Equatorial spread-F characteristics using HF Doppler shift measurements: results from upgraded Doppler sounder system in Tucuman, Argentina

Habtamu Marew[1*], Jaroslav Chum[1], Maria Graciela Molina[2,3,4], Uma Ashrani[5] and Carlos Martinis[5]

Abstract

Horizontals drifts of equatorial Spread F (ESF) at post-sunset and post-midnight are investigated by analyzing six ESF events observed during the period of November 2022–March 2023. Horizontal drift velocities of ESFs are calculated from the time lags between signals recorded by different transmitter–receiver pairs of a new Continuous Doppler Sounding (CDS) system operating at 6.80 MHz in a low latitude station, Tucumán, Argentina (26° 49′ S, 65° 13′ W, mag. latitude ~ 13°) and by the older CDS system working at 4.63 MHz. A new method of time lags determination for spread structures is presented. In addition, the occurrence of airglow depletions associated with ESF events is verified using images of airglow emissions of atomic O red line, 630 nm. We found that the typical speeds of the ESF drift in the post-sunset hours (around 130 m/s) are about two times greater than the speeds of ESF occurring around midnight or in post-midnight hours (around 80 m/s). The drift speeds obtained using 4.63 and 6.80 MHz systems were practically the same with the exception of one event, which might have been due to wind shear. Azimuths obtained by 4.63 and 6.80 MHz systems are almost similar. No systematic dependence of the azimuth on the local time and sounding frequency was found. All ESF events drift roughly eastward with an average azimuth of about 105° with respect to the geographic north.

Keywords Equatorial spread F, Continuous Doppler sounder, Time delays, Airglow images

---

*Correspondence:
Habtamu Marew
alemu@ufa.cas.cz
Full list of author information is available at the end of the article

Graphical Abstract

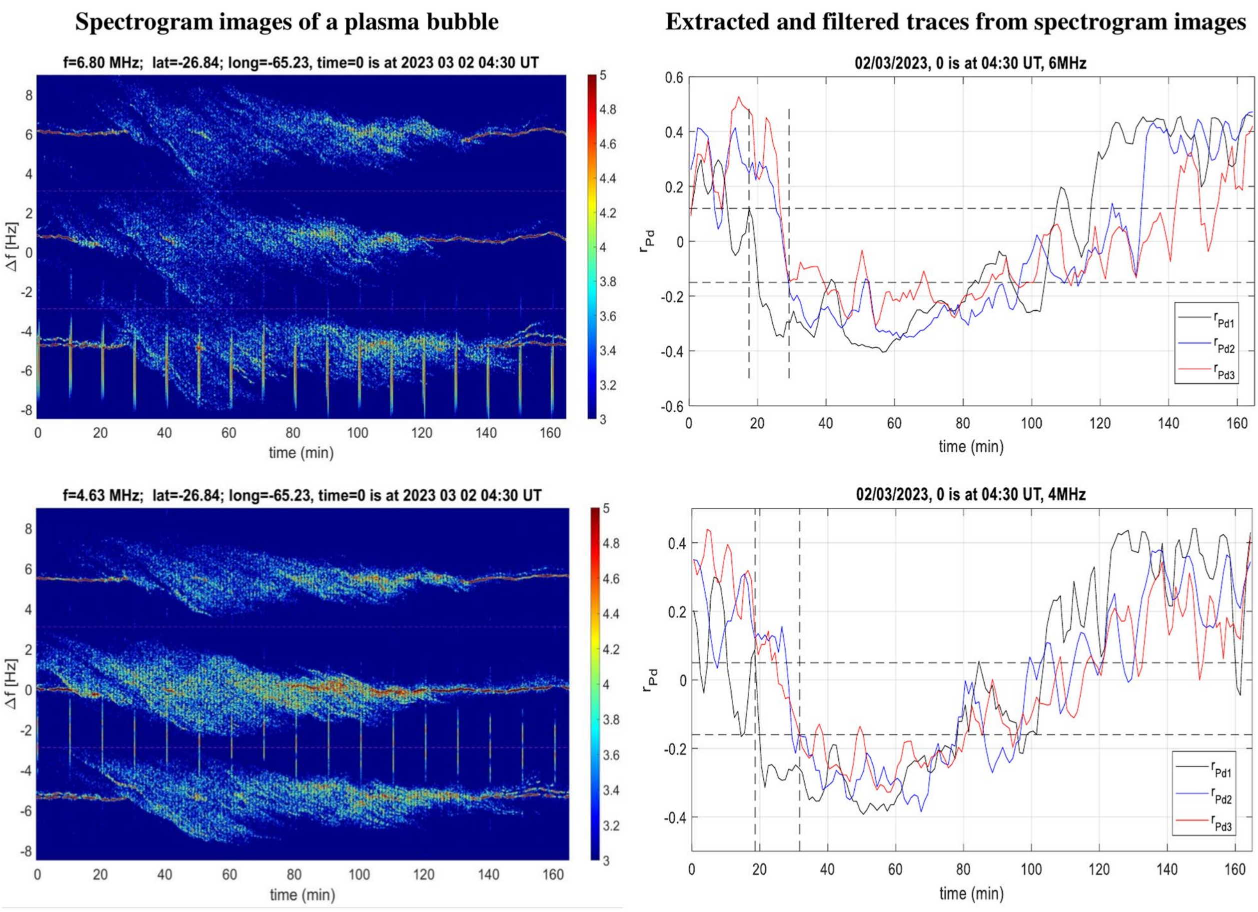

1 Introduction

Electron density irregularities at night in the F region ionosphere cause spreads in range and frequency in radio echoes from the ionosphere. This phenomenon in the equatorial region is called "equatorial Spread F (ESF)". The major sources of ESF are equatorial plasma bubbles (EPBs). EPBs develop within hundreds of kilometers in the east–west direction, thousands of kilometers in the north–south direction, at altitudes of hundreds of kilometers (Kil 2015; 2022). A condition for the development of the post-sunset plasma bubble is the uplift of the evening F layer (Fejer et al., 1999; Abdu et al. 2009). The Rayleigh–Taylor instability (RTI) in the post-sunset period is the cause for the generation of irregularities that are detected as Spread F in ionograms (Meenakshi, et al. 2022). As other forces as well as gravity is involved in the RTI instability, let's define RTI as "generalized RTI" and then use RTI hereafter. Gravitational RTI is effective in the bottomside F region where the electron density gradient and gravitational force directions are opposite. The equatorial ExB drift acting against gravity also contributes to the development and growth of RTI (Meenakshi, et al. 2022). Although not a periodic or usual event, ESF can also occur during daytime hours as a result of geomagnetic storms (Jiang et al. 2015, 2016). The creation of bubbles by the RTI is briefly described by Kil, (2015). Different types of instruments and techniques have been applied to study ionospheric plasma irregularities and plasma bubbles. For instance, airglow equipment has been used by different researchers (e.g., Makela and Kelley 2003; Sekar et al., 2008: Martinis et al. 2010). Irregularities are also investigated using spaced GNSS receivers over Brazil (12.8°S magnetic latitude) by Cesaroni et al., (2021). Their results showed that the ESF drift velocity increases right after the local sunset and shows a smooth decrease in the next hours.

ESF plays a negative role in the quality of trans-ionospheric signal propagation and it has been extensively studied in the last four to five decades (e.g., Fejer and Kelley 1980; Haase et al. 2011; and Chum et al. 2014; 2016). It diffracts radio waves and affects the navigation and communication signals in the equatorial and low latitudes (Panda et al. 2019). Vertical plasma bubble growth supported by weak transequatorial wind has been reported by Abdu et al., (2009). Furthermore, they explained that pre-reversal enhancement of vertical plasma drift provides a favorable condition for ESF development. While an overall understanding of the EPBs structure development and drift direction has been achieved, ESF/EPB climatology, seed perturbations and seed growth in the global scale are topics that need further investigations. Recently, Shinbori et al., (2023) demonstrated volcanic eruption contribution to the development of air pressure waves which in turn are playing a role of seeding for irregularities (EPBs). Another study on the occurrence of ESF/EPB during the post-midnight hours related their occurrence to medium-scale traveling ionospheric disturbances (TIDs) as a seeding source and main driver for irregularities from 00:00 LT to 05:00 LT (Jiang et al. 2015). TIDs triggered by strong tropospheric convective activity are also reported as a seeding source for the occurrences of EPBs in the afternoon to evening period (Takahashi et al. 2018).

Various studies characterized and reported the drift direction and horizontal velocity of ESF/EPBs phenomena using different approaches (Chum et al. 2014; 2016; Qiang et al. 2021; Cândido et al. 2008; Taori et al. 2015; Figueiredo et al. 2018). For instance, Qiang et al., (2021) studied the characteristics of EPBs using satellite observations of the Global Positioning System (GPS) and BeiDou Navigation Satellite System (BDS). A case study by Haase et al., (2011) over the Brazilian sector reported propagation direction of low latitude plasma depletions towards the east with a westward tilt due to the vertical wind shear. They used combination of observations of 630.0 nm airglow images and GPS data from Fazenda Isabel in central Brazil (3.3 ° S, 43.5 ° W). They determined depletion velocities in the range of 85–110 m/s.

For the first time, a multipoint continuous Doppler sounder (CDS) has been used to study ESF/EPB by Chum et al., (2014). They showed the occurrence of ESF as an oblique spread structure (OSS) in Doppler shift spectrograms. The advantage of this new technique relies on the independence from atmospheric weather conditions. Their results indicate that EPB drifts roughly eastward with the mean horizontal velocity around 133 m/s (with standard deviation of 23 m/s) over Tucumán, Argentina. In a following work by Chum et al., (2016), the mean horizontal drift velocity over Taiwan was found to be about 107 m/s. In addition, high-frequency (HF) Doppler sounders provide broad opportunity to characterize the traveling ionospheric disturbance (TID) lasting from periods of 1 min to over an hour (Crowley and Rodrigues 2012; Chum et al. 2014). Recently Sejima et al., (2023) compared the OSS observed in Doppler shift spectrograms, including their fine structure, with simultaneous O red line (630 nm) air glow observation of EPB over Taiwan and proved the OSS corresponds well with the EPB occurrence in air glow images.

The determination of drift speeds using the CDS system was based on the time delays between each trace from the three transmitters or on the tilt of the spread structures in the Doppler shift spectrograms (Chum et al. 2016). However, the determination of the time lags/delays and the tilts was a bit subjective, based on the visual inspection and manual clicking by mouse at the specific locations in the Doppler shift spectrograms and readings of the corresponding coordinates (Doppler shifts and times). Therefore, we introduce a new technique for determining the time lags. In addition to the existing 4.63 MHz CDS system, we also use a new CDS system with 6.80 MHz transmitters. Our work includes comparison of the characteristics of ESF using dual frequency CDS systems over Tucumán which has not been done before. Because the two frequencies reflect from different heights in the ionosphere, dual frequency analysis increases our understanding of drift speed and direction of the same ESF structure at different altitudes. Dual analyses are done for ESF structures observed on both 4.63 and 6.80 MHz spectrograms. Moreover, the occurrence of EPBs is verified by simultaneous airglow measurements.

2 Observation and data

In this study, we analyzed six ESF events in Tucumán, Argentina, observed during the period of November 2022–March 2023 using the CDS systems operating at frequencies of 4.63 and 6.80 MHz. The 4.63 MHz system has been working since the end of 2012. The 6.80 MHz CDS system was installed in October 2022 and the measurements at this frequency are used for the first time in this study. Each of these two systems consists of three transmitters and one receiver. The three transmitters of each CDS system are located in a triangular arrangement; see the points of reflection (not locations of the transmitters) in the ionosphere when projected onto the ground in Fig. 1a. The transmitters and receivers of the 4.63 and 6.80 MHz systems are co-located. More detailed description of the CDS system characteristics is presented in Chum et al. (2010, 2012 and 2014). To compare the ESF events and their drift speeds observed during the post-sunset hours and around the post-midnight hours, we systematically selected three events for each case (i.e., three events

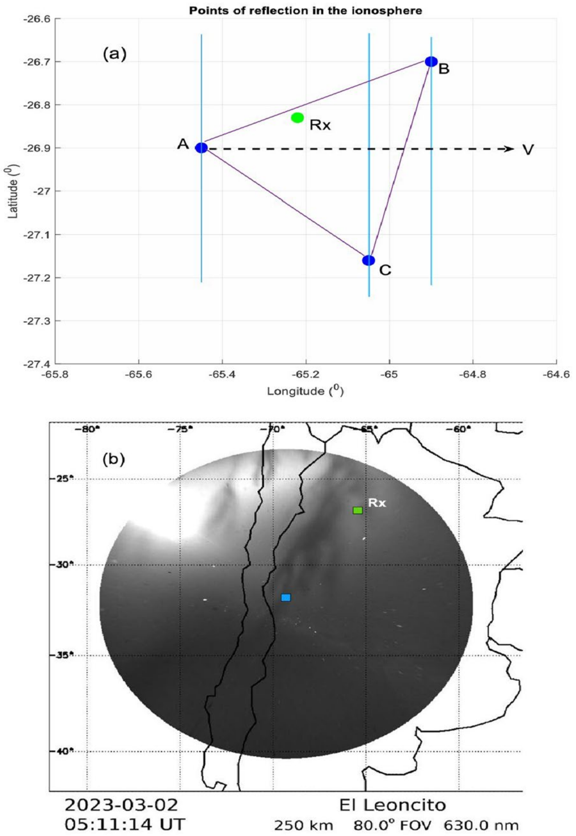

Fig. 1 **a** Is a schematic diagram of ESF disturbance fronts and points of reflection in the ionosphere. On the triangle ABC, A stands for a reflection point in the ionosphere of the transmitter 1 projected on the ground; **B** stands for reflection point of the transmitter 2; **C** stands for reflection point of the transmitter 3. The broken line with an arrow indicates the direction of apparent velocity (V) of the Spread-F structure. **b** An 630.0 nm airglow image from El Leoncito, Argentina, recorded at 05:11:14 UT on 02–03-2023. The blue square indicates the zenith location of the All-Sky Imager and the green square (Rx) is the location of Tucuman CDS system receiver, indicated in panel a by a green dot (Rx)

from the post-sunset and three events from the post-midnight hours). The six events selected are characterized by distinct OSS, are not interfered significantly by signals from other sources (e.g., ionosonde signal) and are observed simultaneously on both frequencies (4.63 and 6.80 MHz). In addition, these events have a sharp front part, which makes the determination of time lags between observation by different transmitter–receiver pairs possible (see also Section 3). The requirement of sharp fronts is a limitation of the method used to obtain the drift speed and direction. To confirm that the ESF structures observed in Doppler shift spectrograms are caused by EPBs, we also checked the available airglow observation of atomic oxygen (O) red line emissions (630 nm) from an All-Sky Imager (ASI) located at El Leoncito Observatory, Argentina (31.8 ° S, 69.3 ° W, −18 ° mag. latitude) (Martinis et al. 2006, 2018). Due to cloudy conditions or moon light contamination, not all the events recorded by CDS could be compared with ASI-airglow observations. More explanations are presented below in Sect. 4.

Figure 1b shows an unwrapped image at 05:11:14 UT on 2 March 2023 obtained by the ASI, assuming an emission height of 250 km. The zenith location is shown as a blue square and the location of the Tucuman CDS system receiver as a green square. Several airglow depletions associated with ESF can be observed on the image.

The objective of our study is to present a new technique of determining the time lags between observation of corresponding ESF structures on different transmitter–receiver pairs and to determine the horizontal drift velocity from the time lags. As mentioned above, we selected events from post-sunset hours and around post-midnight hours to investigate the possible difference in the speed of the structures depending on the local time. The midnight (00:00 LT) in Tucuman, Argentina, is at about 04:00 UT. The events on 06–11-2022 (01:30–03:30 UT); 07–11-2022 (02:15–04:00 UT); and 09–11-2022 (00:00–01:45 UT) represent the after sunset hours, whereas the events on 07–11-2022 (04:15–07:00 UT); 16–11-2022 (04:00–07:20 UT); and 02–03-2023 (04:30–06:15 UT) represent the post-midnight spread structures. All data selection and processing are done for both frequencies (i.e., 4.63 MHz and 6.80 MHz). Since the reflection heights for two frequencies are different and are of random property for ESF, we do not cross-correlate the signals across frequencies as was done in the case of 3D propagation analysis of travelling ionospheric disturbances associated with gravity waves (Chum and Podolska, 2018; Chum et al. 2021), but we provide and compare the results obtained separately for each frequency. An example of the post-midnight event is presented in Fig. 2. The ESF events are seen as tilted/oblique spread structures in the Doppler shift spectrograms. The vertical lines (structures) that recur regularly every 10 min in Fig. 2 are caused by interference with a nearby ionosonde.

3 CDS data analysis

Basically, the analysis can be grouped into two main parts: (i) the calculation of time lags (delays) and (ii) horizontal velocity determination. By the time delay we mean the time difference between the passage of the same disturbance (ESF in this case) or its part through two different reflection points. For instance, from Fig. 1a, the time lag for a disturbance crossing point A and point B is designated by τ_{AB}. Similarly, τ_{AC} represents the time difference for a disturbance front to reach from point A to

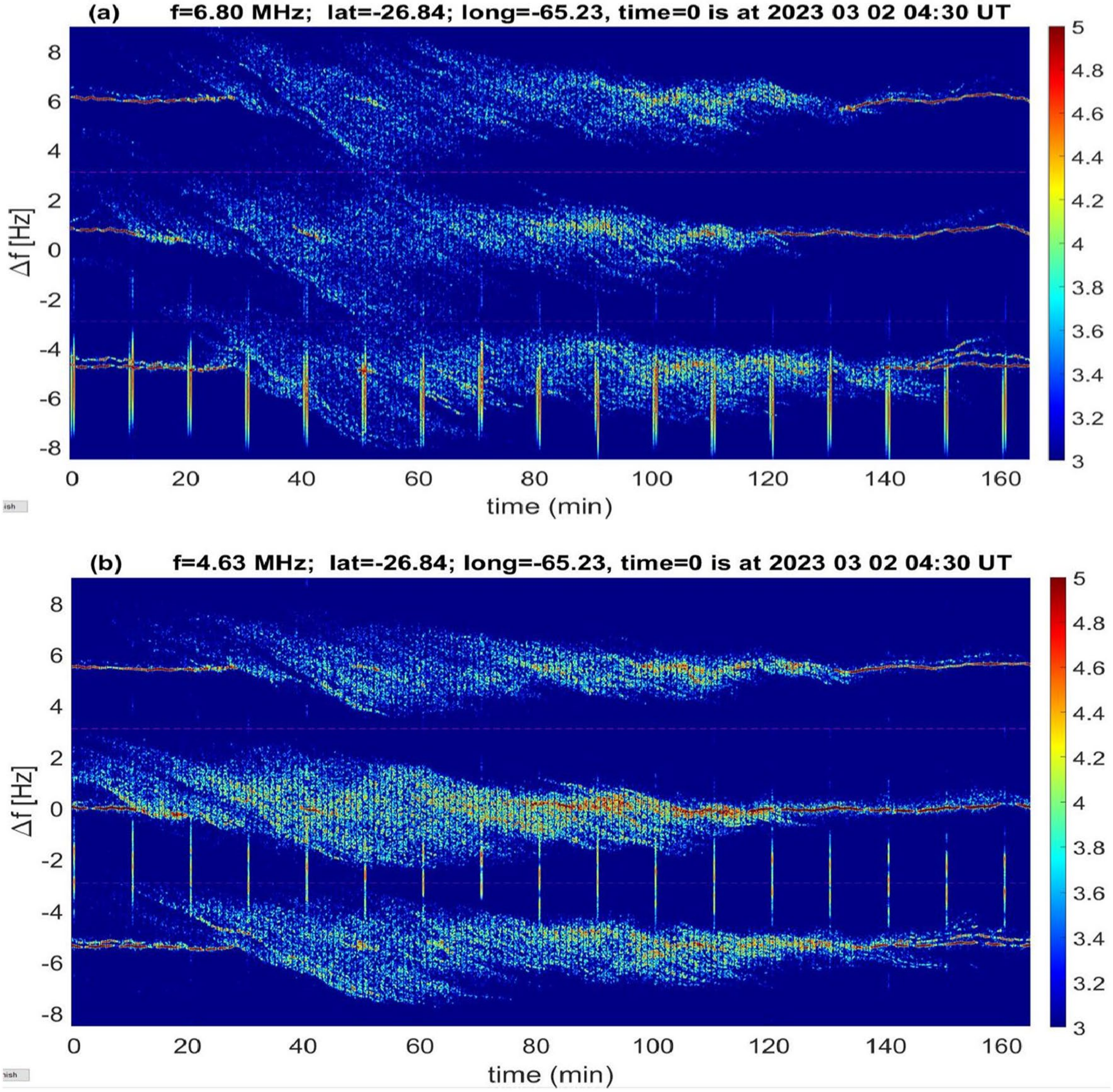

Fig. 2 Doppler shift spectrograms recorded on 02–03-2023 from 04:30 to 06:15 UT, by 6.80 MHz receiver (top panel) and 4.63 MHz receiver (bottom panel) over Tucumán, Argentina. The color indicates the Common logarithm of power spectral densities of the received signals in arbitrary units (the antennas are not calibrated)

point C and τ_{CB} is the time lag between the observation disturbance front at the point C and B, respectively.

A fast Fourier transform (FFT) with sliding cosine window is employed to produce smooth Doppler shift spectrogram (Fig. 2). The spectrogram shows the power spectral densities and Doppler shift for signals received from each transmitter of the CDS systems. To determine the time delays between the observation of the ESF structure at different reflection points, we evaluate the spectral density peak "quality" as a function of time for each signal (transmitter–receiver pair) by calculating the ratios *r:*

$$r = \frac{P_N}{P_W}, \quad (1)$$

where P_N is the signal power in a narrow band (~0.1 Hz) around the spectral density maximum for each transmitter, and P_W is the power in a wide frequency band that includes the whole ESF structure for the same transmitter (P_W is obtained for about 4 Hz wide band – see the spectrograms). At each instant of time on the spectrogram, the peak is determined by the ratio defined by Eq. (1). The values of r are in the range $0 \le r \le 1$ and an example of ratios r_1, r_2 and r_3 obtained for the event shown in Fig. 2 is presented in Fig. 3 (the indices 1, 2, 3 denote

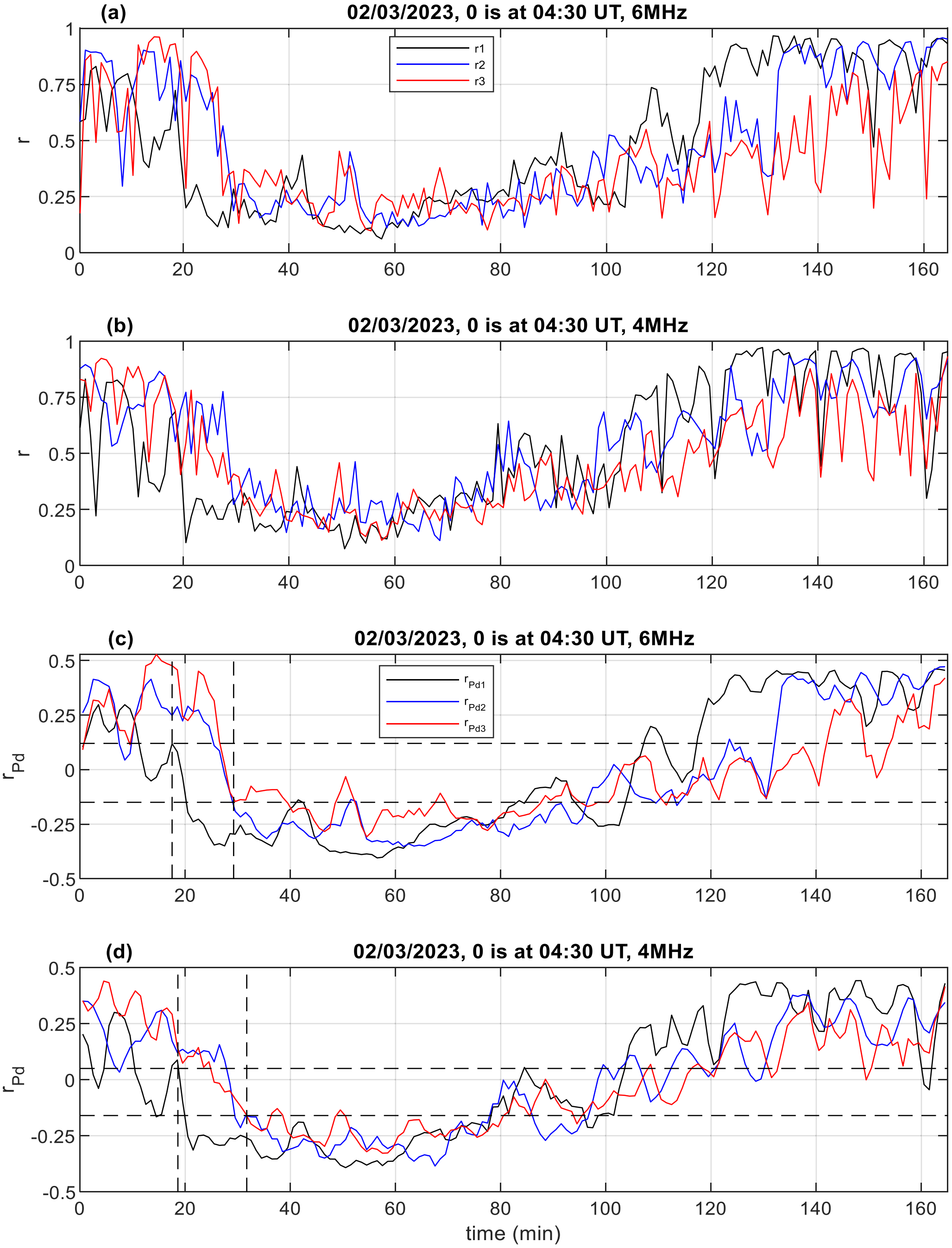

Fig. 3 Ratios for a Spread F occurred post-midnight on 02-03-2023 (from 04:30–06:15 UT). The top two panels are for un-smoothed CDS signals. Three signals from three transmitters: r_1 (black), r_2 (blue) and r_3 (red) are presented to each receiver (panels **a** & **b**). In the bottom two panels (**c** & **d**), the curves: r_{Pd} (black), r_{Pd} (blue) and r_{Pd} (red) are obtained applying Eq. (2) and smoothed for convenient analysis and interpolated for better time resolution. In addition, the parts of the traces used to calculate the time lags (delays) are indicated with a box formed by the interception of the four broken lines of vertical limits (ratios) and horizontal limits (time). Similar supporting figures are also available for the other five events in Additional file 1

the signals from the transmitters 1, 2, 3, respectively). The ratios have large values when clear signal is received (distinct peak of power spectral density) and low values during very diffused ESF occurrence. During the periods of ESF, the Doppler traces are very much diffuse/spread and the frequency of the spectral density maximum can jump randomly. However, the ratios r remain low due to the large spectral width of the OSS. There is no distinct narrow peak of power spectral density during ESF and $P_N << P_W$. In the time periods in which ESF does not occur and distinct peak in spectrum is observed, P_W is approximately the sum of the power of the reflected signal (P_N) and some noise. The ratios r_1, r_2 and r_3 displayed in Fig. 3a & b and figures presented in Additional file 1 exhibit large fluctuations, which makes determination of the time delays difficult. Therefore, we calculated running average using a time window of [-1 min, 1 min] to reduce the fluctuations and to obtain smooth ratios r_F. In addition, we also subtracted the mean values r_{mean} calculated over the whole selected interval (165 min in the example shown in Fig. 3). The obtained ratios r_{Pd} obtained for the ratios r_F (using Eq. 2) are displayed in Fig. 3c & d:

$$r_{Pd} = r_F - r_{mean} \tag{2}$$

It is worth noting that the time of the drop (falling edges) of the ratios r_{Pd} (Fig. 3) corresponds with the times of front edges of the OSSs in the Doppler shift spectrogram (Fig. 2). We have also compared the velocities obtained for ratios using Eq. (2) with the results obtained for the normalized ratios (r_{Nd}) defined by Eq. (3):

$$r_{Nd} = \frac{r_F - r_{mean}}{\sigma(r_F)}, \tag{3}$$

where $\sigma(r_F)$ is the standard deviation of r_F. The normalization could help and affect the obtained time delays in the case of different strengths of the signals received from various transmitters. This is usually not the case and the results differ negligibly as will be shown in the section 5.

Next, we selected a time interval in which the ratios r_{Pd1}, r_{Pd2}, and r_{Pd3} decrease smoothly, almost linearly, from high to low values.

The time delays between the curves in the selected time intervals are obtained as follows. First, the ratios r_{Pd1}, r_{Pd2}, and r_{Pd3} were interpolated from 1-min resolution to a time step of 0.1 min for better time resolution. Next, the time delays τ_{AB}, τ_{AC}, τ_{CB} were determined for various values of r_{Pd} with the step of 0.01 (along the vertical axis) inside the marked box. For each value of r_{Pd} along the marked box (Fig. 3c & d), changed with the step 0.01, we subsequently searched for the times t_1, t_2 and t_3 at which the ratios r_{Pd1}, r_{Pd2}, and r_{Pd3} cross the selected r_{Pd}. The time delays τ_{AB}, τ_{AC} and τ_{CB} are determined as the time differences t_1-t_2, t_1—t_3 and t_2—t_3, respectively. It should be noted that we obtained several (around 30) different time delays τ_{AB}, τ_{AC} and τ_{CB}. Using different values of the τ_{AB}, τ_{AC} and τ_{CB} in the calculation of horizontal velocities allows estimating uncertainties. The method described above for determining τ_{AB}, τ_{AC} and τ_{CB} was found to be more reliable than finding the times of maxima of the cross-correlation functions because the latter one depends on the length of the selected interval. It should also be noted that neither the method described above nor the cross-correlation provides usable results for the periods after the passage of the front edges of the OSSs (the rear edge may be used in few cases, however, it is usually not sharp enough).

The horizontal drift velocities are calculated from the obtained time delays and distances between each pair of the reflection points (Fig. 1a). The distances are decomposed into two perpendicular components and the velocities are calculated by the least square solution (Chum and Podolská, 2018, Eq. 3). The standard deviations of the ESF drift speeds are determined from the multiple least square solutions obtained for various time delays corresponding to different r_{Pd} values.

4 ASI observations

Figure 4 shows airglow images on 2 March 2023, corresponding to the event presented in Fig. 2. Images were processed assuming an emission height of 250 km and zenith angles less than 80 deg. As in Fig. 1b, blue square indicates the location of El Leoncito ASI and green square shows the location of Tucuman CDS system. A small depletion is moving over Tucuman between ~ 3:30 UT and 4:00 UT. Around 5:00 UT another depleted structure is seen over Tucuman which corresponds to the front edge of oblique structure in Fig. 2. Figure 4 also shows that the analyzed EPB extended up to a latitude of about 33°S.

The sequence of images demonstrates that the structure of the EPBs drifted roughly eastward. By taking 10 pixels wide east–west horizontal cuts centered at the location of Tucuman CDS, a keogram is constructed to infer the zonal motion of the depletions (Martinis et al. 2003). The depletions moving through the location of Tucuman between ~ 5:00 and ~ 6:00 UT have a speed of ~ 70 ± 10 m/s. We were also able to determine the zonal speed for the 16 Nov 2022. The average speed obtained between 04:00 and 05:00 was 80 m/s and between 05:00–07:00 was 67 m/s.

5 Results

As described in the data section, for this study we have used six ESF events observed in Tucumán, Argentina. The ESF horizontal drift speeds (*Vh*) are calculated for three selected post-sunset events and three post-midnight events using the methods explained above. The time span of the events ranges from 105 to 200 min. The obtained drift speeds are summarized in Table 1. Time lags have been determined for ratios obtained using both Eq. (2) and (3). As can be seen in Table 1, the

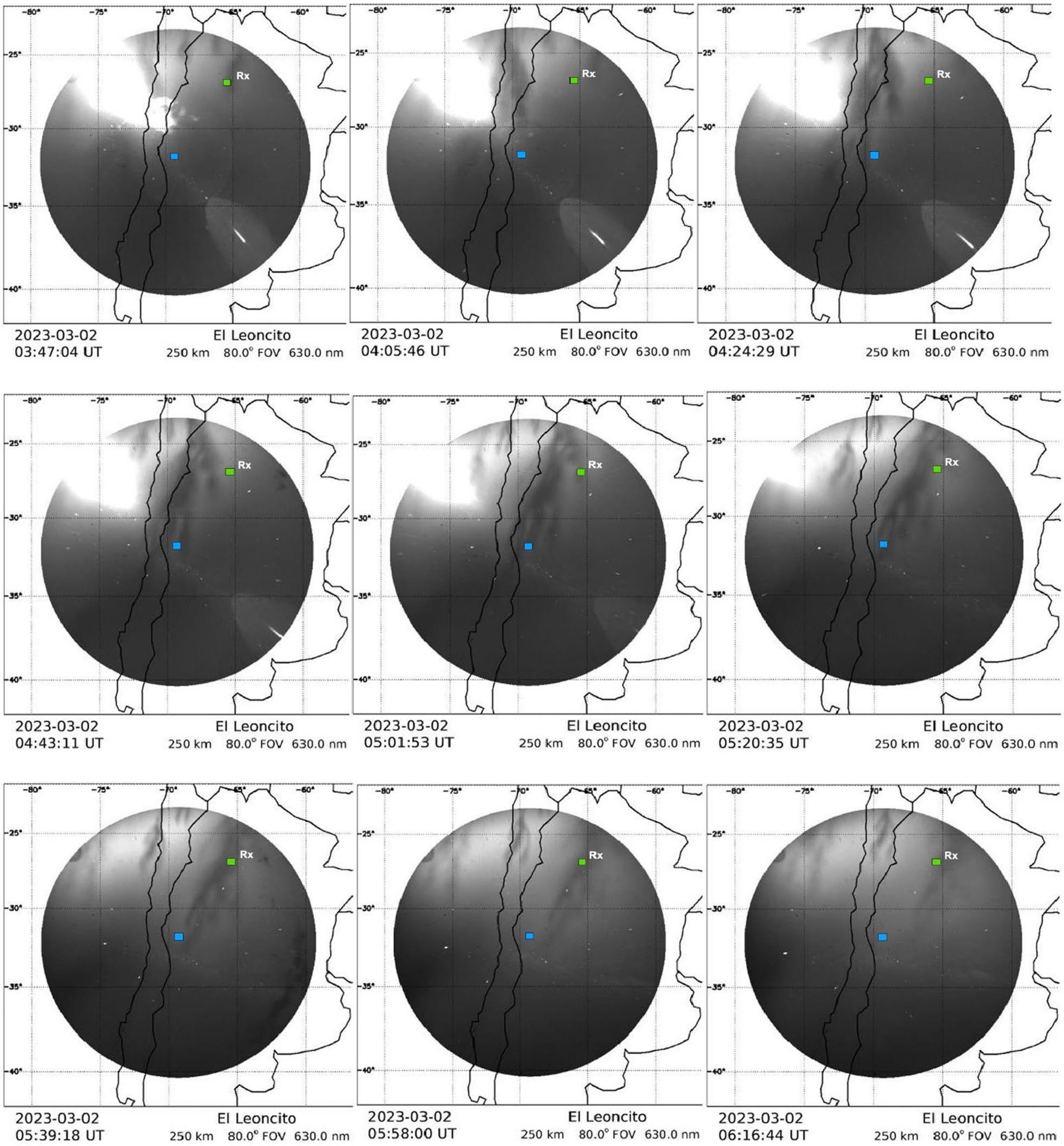

Fig. 4 630.0 nm All-Sky airglow images of ESF event on 02–03-2023 observed over El Leoncito, Argentina. The sequence of images demonstrates that the airglow depletions drifted eastward. The radius for the zenith angle 80° and approximate emission height of 250 km is about 1000 km. Detail illustration is available in a movie format under Additional file 2

obtained drifts speeds range from 80 to 160 m/s, which is consistent with the drift speeds of EPB presented by Haase et al. (2011) and Chum et al. (2014). On average, the disturbance speeds of the post-sunset hour events (1–3) are approximately two times greater than the speeds of post-midnight hour events (4–6). The average post-sunset ESF/bubble speed calculated using Eq. (2) and the new CDS system (6.80 MHz) is ~ 130 m/s, whereas the average post-midnight ESF/bubble speed is 80 m/s. The results obtained using Eq. (3) are very similar to those obtained using Eq. (2).

Table 1 Horizontal drift speed of ESF events with the corresponding standard deviations (σ_{vh}) obtained using Eqs. (2 and 3)

Events	Date and time (UT = LT + 4.3)	Results using Eq. (2)				Results using Eq. (3)			
		6.80 MHz		*4.63 MHz*		*6.80 MHz*		*4.63 MHz*	
		Vh (m/s)	σ_{vh}*(m/s)*	*Vh (m/s)*	σ_{vh}*(m/s)*	*Vh (m/s)*	σ_{vh}*(m/s)*	*Vh (m/s)*	σ_{vh}*(m/s)*
1	06-11-2022, 01:30–03:30	133	8	131	16	134	8	129	15
2	07-11-2022, 02:15-04:00	98	7	77	16	98	5	77	14
3	09-11-2022, 00:00-01:45	156	33	157	32	151	32	153	24
4	07-11-2022, 04:15-07:00	80	2	79	5	80	3	78	5
5	16-11-2022, 04:00-07:20	68	9	91	24	68	7	90	21
6	02-03-2023, 04:30-06:15	96	3	90	14	96	2	93	12

Tables 1 and 2 show that the speeds obtained by the CDS system on 2 March 2023 are ~ 96 ± 3 m/s and ~ 91 ± 15 m/s with azimuth of 109° and 101° (clockwise from the geographic north) for 6.8 and 4.63 MHz, respectively. Considering the magnetic field declination (about -7.3° at the altitude of 260 km), the measured propagation azimuth with respect to the magnetic field line is about 7.3° larger over Tucumán. The average zonal speed determined between ~ 04:30–05:00 UT (i.e., UT = LT + 4.3) on 2 March 2023 using the All-Sky images (assumed azimuth of the horizontal drift 90°) is about 90 m/s. This is fully consistent with the speed estimated using the CDS. 30-min averages of ESF velocities derived from airglow images are presented in Fig. 5. As indicated in the legend "red triangle" is for velocity obtain from CDS (V_{CDS}). Figure 5 confirms the decrease of EPB drift velocities with time (lower velocities are observed in post-midnight hours than after sunset).

As explained in Park and Luhr (2013) and Liu et al. (2009), the dynamics of winds affects the horizontal drift speed of EPBs. Chapagain et al. (2013) stated that the nighttime eastward winds, EPBs velocities, and plasma drifts increase in the early evening hours, and decrease in the local midnight and post-midnight periods. Chum et al (2014; 2016) also reported similar conclusion based on Doppler sounder observations and stated that ESF velocity tends to decrease after ~ 04:00 UT over Tucuman. Therefore, slow drift of the post-midnight EPBs is probably due to the decrease of eastward neutral wind.

The estimated height of reflections for 4.63 and 6.8 MHz signals for this post-midnight event and basic ionospheric characteristics obtained from the ionosonde located in Tucumán are presented in Table 3. The abbreviations, *hmF2* and *h'F2* and *foF2* represent the F2-layer peak height, the starting height of F2 layer and the critical frequency of the F2 layer, respectively, of the F2-layer. The apparently missing observation in Table 3 corresponds to intense ESF, so it was impossible to get reliable heights. It should be noted uncertainties in height determination during the ESF conditions may be quite large (several 10 km).

The drift speeds obtained using the 4.63 MHz system are very similar to those obtained by the 6.80 MHz system except for the event 5 (16 Nov 2022), for which the speeds of ~ 90 m/s and ~ 70 m/s were obtained using 4.63 MHz and 6.80 MHz systems, respectively. This large difference may arise from altitudinal variations in neutral winds and electron density dynamics during this specific event. Figure 6 clearly shows the large discrepancies between the time delays detected by 6.80 MHz and 4.63 MHz systems. Figure 6a (6.80 MHz) shows large

Table 2 Azimuth of ESF events with the corresponding standard deviations (σ_{ϕ}) obtained using Eqs. (2 and 3)

Events	Results using Eq. (2)				Results using Eq. (3)			
	6.80 MHz		*4.63 MHz*		*6.80 MHz*		*4.63 MHz*	
	ϕ(°)	σ_{ϕ}(°)	ϕ(°)	σ_{ϕ}(°)	ϕ(°)	σ_{ϕ}(°)	ϕ(°)	σ_{ϕ}(°)
1	102	13	93	5	103	13	94	6
2	116	6	118	12	115	7	118	10
3	129	8	131	15	129	7	122	14
4	111	0.3	109	1	109	3	109	6
5	93	21	99	7	87	23	100	4
6	110	2	102	12	108	2	100	11

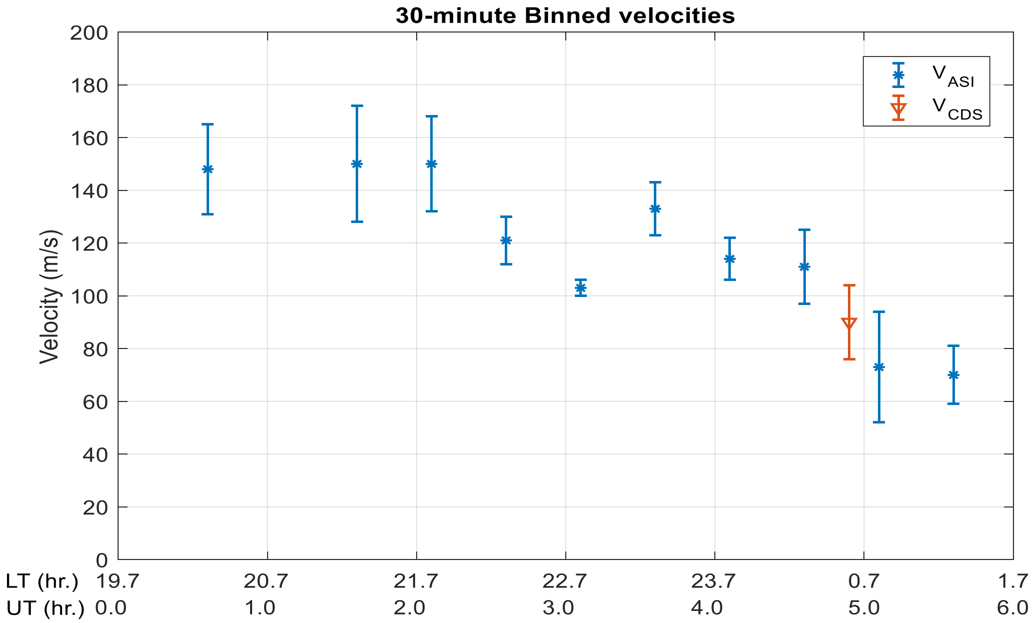

Fig. 5 A 30-min average horizontal drift velocities of an EPB occurred on 2 March 2023. As indicated in the legend "blue star" is for velocity derived from ASI (V_{ASI}) and "red triangle" is for velocity obtain from CDS (V_{CDS}). Note that UT = LT + 4.3

Table 3 Ionosonde height *(h)* profile for 4.65 MHz and 6.8 MHz reflections for a post-midnight event occurred on 02-03-2023

Date and time	*hmF2* (km)	*foF2* (MHz)	*h'F2* (km)	~ *h* (km)	
				For 4.65 MHz	For 6.80 MHz
2023-03-02 03:00:00	345	13.7	260	–	280
2023-03-02 03:10:00	342	13.3	260	270	280
2023-03-02 03:20:00	323	12.9	250	260	280
2023-03-02 04:00:00	324	12.9	250	260	270
2023-03-02 04:10:00	350	13.1	250	260	280
2023-03-02 04:20:00	331	12.9	250	260	270
2023-03-02 04:30:00	321	13.1	250	260	280
2023-03-02 04:40:00	315	13.3	240	250	270
2023-03-02 06:50:00	272	11.2	220	240	260

The abbreviations, *hmF2* and *h'F2* and *foF2* represent the peak height, the starting height and the critical frequency, respectively, of the F2-layer of the ionosphere. The apparently missing observation corresponds to intense ESF, so it was impossible to get reliable heights

time delays between the r_{Pd1} and r_{Pd2}, r_{Pd3} compared to time delays shown in Fig. 6b (4.63 MHz). We were able to determine the zonal speed for the 16 Nov 2022 using the airglow observations from El Leoncito ASI. The average speed obtained between 04:00 and 05:00 UT was 80 m/s which is consistent to the result obtained by the 4.63 MHz CDS (~ 90 ± 24 m/s) and reasonably close to the value obtained by the 6.8 MHz CDS (~ 68 ± 9 m/s).

As shown in Table 2, the azimuth of the horizontal drift of the analyzed ESF events obtained from the new 6.80 MHz CDS system varies between ~ 90 ° and ~ 130 ° with an average azimuth of 110 °. Unlike, the drift velocities, no systematic dependence of azimuth on local time was found. The roughly eastward drift of ESF structure for the event that occurred on 2 March 2023 can also be confirmed by the sequence of images shown in Fig. 4. Watch the movie in Additional file 2 for a better time resolution of the ASI images. Specifically, for this event we obtained relatively small differences of azimuths obtained from 4.6 MHz (~ 101 ± 12°) and 6.8 MHz (~ 109 ± 3°) systems, reflecting at different heights. Sometimes wind shear could be responsible for a slight azimuthal difference because, the direction of neutral winds mainly controls the drift velocity vector. EPBs seen from space show

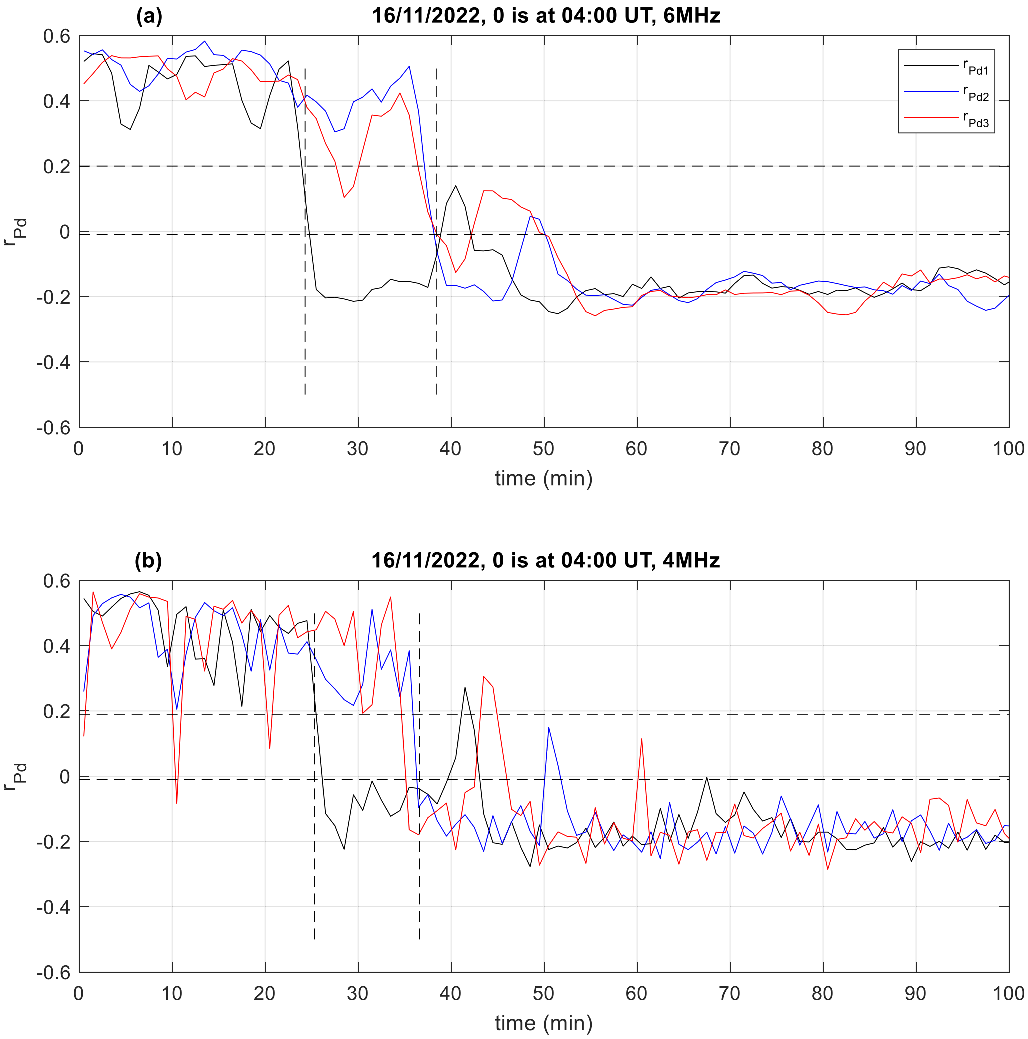

Fig. 6 The half or zoom in signal plot of ratios for event 5 mentioned in Tables 2 and 3. Top panel (6.80 MHz) shows large time delays between r_{Pd1} and r_{Pd2}, r_{Pd3} when compared to what the disturbance signal traces show on bottom panel (4.63 MHz)

backward C-shaped structures (Kil 2015). If the shape of the structure/EPB changes with local time, the velocity/azimuth calculations might be affected (see Zalesak et al. 1982 and Patil et al. 2023). The slightly southeastward drift directions of most of the events we analyzed in this manuscript may manifest the backward C-shaped structure of bubbles. For instance, Zalesak et al. (1982) suggested a theory that makes an incomplete coupling of plasma motion with neutral wind responsible for the backward C-shaped drifting of the EPBS. Kil (2015) demonstrated that differential zonal plasma drift velocity (plasma in the inner flux tubes, which are closer to the equator drift faster than in the outer flux tubes) will result in the backward C-shape and the westward tilt of the upper part of the EPB. It is possible that the observation of azimuths slightly larger than ~ 90 ° is due to the out of equatorial location of Tucumán and the backward C-shape of the EPB. Usable ASI-airglow images of EPB are available only for the event on 02-03-2023 (due to the local observation, CDS is not usable to observe the shape of the EPB). The complete backward C-shape cannot be detected in the images because the field of view does not cover the whole EPB. Nevertheless, the EPB is clearly not aligned along the meridian, but tilted eastward closer to the equator and westward in its southern edge, which is consistent with the backward C-shape. As can be seen in Table 2, the azimuth determined by CDS for this event is ~ 109^0 at the 6.80 MHz reflection altitude and ~ 101^0 at 4.63 MHz reflection altitude. As mentioned, no systematic dependence of azimuth on local time was observed, however, it seems that the variability of azimuths is lower for the post-midnight events. Kil (2015) mentioned that multiple factors play a role in formation of EPBs. Obviously, worldwide long-term observations based on complementary observation techniques are necessary to fully describe the climatology and variability of EPBs.

6 Conclusion

We presented a new technique of determining the time lags to calculate the drift speeds of ESF/EPBs using both the existing 4.63 MHz and the new CDS system operating at 6.80 MHz in Tucumán, Argentina. The occurrence of EPBs of two ESF events were verified by 630.0 nm airglow images from an All-Sky Imager at El Leoncito Observatory. The drift speeds, obtained with the proposed method during the post-sunset hours are greater, ~ 100 – 160 m/s, than the speeds of post-midnight hour events, which usually drift with a horizontal velocity between ~ 60 and 90 m/s. The drift speeds obtained using 4.63 and 6.80 MHz systems were practically the same with an exception for one event that occurred on 16 November 2022 (04:00–07:20 UT). Azimuths of drift of the analyzed ESF events range from 87 ° to 131 ° with an average of 105 ° with respect to the geographic north. Unlike, the drift velocities, no systematic dependence of azimuth on local time was found. The new technique will enable future statistical analyses of ESF horizontal drift characteristics and the search for non-standard events.

Abbreviations

ASI	All-sky imager
ESF	Equatorial spread F
CDS	Continuous Doppler sounding
RTI	Rayleigh–Taylor instability
EPBs	Equatorial plasma bubbles
TIDs	Traveling ionospheric disturbances
GPS	Global positioning system
BDS	BeiDou navigation satellite system
OSS	Oblique spread structures
HF	High frequency
FFT	Fast Fourier transform
hmF2	F2-layer peak height
h'F2	The starting height of F2 layer
foF2	Critical frequency of the F2 layer

Supplementary Information

The online version contains supplementary material available at https://doi.org/10.1186/s40623-025-02147-3.

Additional file 1. This file contains supporting figures to the Figures 3-4 and Tables 1 and 2.

Additional file 2. This movie contains sliding supporting figures to Figure 5.

Acknowledgements
The Doppler data are available at http://datacenter.ufa.cas.cz/ under the link to spectrogram archive and/or to 8 hours (2 hours) spectrograms. Quick look images and movies from El Leoncito All-Sky Imager can be found at the Boston University Imaging science group website www.buimaging.com. HM acknowledges the support from Czech Academy of Sciences, under grant number 560823AHA. JC and MGM acknowledge the support by the mobility plus CONICET-22-02 project by the Czech Academy of Science and by ESA contract No. 4000143632/24/I-EB (QUID-REGIS). CM and UA work was supported by NSF Aeronomy grant # 2152365. CM thanks the Director and personnel from the Complejo Astronomico El Leoncito (CASLEO) for their continued support of the All-Sky Imager installed at El Leoncito.

Author contributions

HM performed the analysis of the CDS and wrote the manuscript. JC designed the study and helped with the analysis and the manuscript. MGM provided the ionosonde height profiles. CM and UA analyzed and provided airglow images of the All-Sky Imager. All authors read and approved the final manuscript.

Funding
HM acknowledges the support from Czech Academy of Sciences, under grant number 560823AHA. JC and MGM acknowledge the support by the mobility plus CONICET-22-02 project by the Czech Academy of Science and by ESA contract No. 4000143632/24/I-EB (QUID-REGIS). CM and UA work was supported by NSF Aeronomy grant # 2152365.

Availability of data and materials

HF Doppler. The Institute of Atmospheric Physics of the Czech Academy of Science, (http://datacenter.ufa.cas.cz/). Images and movies from El Leoncito All-Sky Imager can be found at the Boston University Imaging science group website (www.buimaging.com).

Declarations

Ethics approval and consent to participate

Not applicable.

Consent for publication

Not applicable.

Competing interests

The authors declare no competing of interest.

Author details
[1]Institute of Atmospheric Physics of the Czech Academy of Sciences, Prague, Czech Republic. [2]Tucumán Space Weather Center, Facueltad de Ciencia Exactas y Tecnología (FACET), Universidad Nacional de Tucumán (UNT), Tucumán, Argentina. [3]Consejo Nacional de Investigaciones Científicas y Técnicas, CONICET, Buenos Aires, Argentina. [4]Istituto Nazionale di Geofisica e Vulcanologia (INGV), Roma, Italy. [5]Center for Space Physics, Boston University, Boston, MA, USA.

Received: 25 June 2024 Accepted: 5 February 2025

References

Abdu MA, Batista IS, Reinisch BW, De Souza JR, Sobral JHA, Pedersen TR, Groves KM (2009) Conjugate point equatorial experiment (COPEX) campaign in Brazil: electrodynamics highlights on spread F development conditions and day-to-day variability. J Geophys Res Space Physics 114:4

Cândido CMN, Pimenta AA, Bittencourt JA, Becker-Guedes F (2008) Statistical analysis of the occurrence of medium-scale traveling ionospheric disturbances over Brazilian low latitudes using OI 6300 nm emission all-sky images. Geophys Res Lett 35:17

Cesaroni C, Spogli L, Franceschi GD, Damaceno JG, Grzesiak M, Vani B, Monico JFG, Romano V, Alfonsi L, Cafaro M (2021) A measure of ionospheric irregularities: zonal velocity and its implications for L-band scintillation at low-latitudes. Earth Planet Phys 5(5):1–12. https://doi.org/10.2646/epp2021042

Chapagain NP, Fisher DJ, Meriwether JW, Chau JL, Makela JJ (2013) Comparison of zonal neutral winds with equatorial plasma bubble and plasma drift velocities. J Geophys Res Space Phys 118:1802–1812. https://doi.org/10.1002/jgra.50238

Chum J, Podolská K (2018) 3D analysis of GW propagation in the ionosphere. Geophys Res Lett 45(21):11–562

Chum J, Šindelářová T, Laštovička J, Hruška F, Burešová D, J. Baše, (2010) Horizontal velocities and propagation directions of gravity waves in the ionosphere over the Czech Republic. J Geophys Res. https://doi.org/10.1029/2010JA015821

Chum J, Hruska F, Zednik J, Lastovicka J (2012) Ionospheric disturbances (infrasound waves) over the Czech Republic excited by the 2011 Tohoku earthquake. J Geophys Res. https://doi.org/10.1029/2012JA017767

Chum J, Bonomi FAM, Fišer J, Cabrera MA, Ezquer RG, Burešová D, Šindelářová T (2014) Propagation of gravity waves and spread F in the low-latitude ionosphere over Tucumán, Argentina, by continuous Doppler sounding: first results. J Geophys Res Space Phys 119(8):6954–6965

Chum J, Liu JY, Chen SP, Cabrera MA, Laštovička J, Baše J, Ezquer R (2016) Spread F occurrence and drift under the crest of the equatorial ionization anomaly from continuous Doppler sounding and FORMOSAT-3/COSMIC scintillation data. Earth, Planets Space 68(1):1–18

Chum J, Podolská K, Rusz J, Baše J, Tedoradze N (2021) Statistical investigation of gravity wave characteristics in the ionosphere. Earth Planets Space 73:60. https://doi.org/10.1186/s40623-021-01379-3

Crowley G, Rodrigues FS (2012) Characteristics of traveling ionospheric disturbances observed by the TIDDBIT sounder. Radio Sci. https://doi.org/10.1029/2011RS004959

Fejer BG, Kelley MC (1980) Ionospheric irregularities. Rev Geophys 18(2):401–454

Fejer BG, Scherliess L, De Paula ER (1999) Effects of the vertical plasma drift velocity on the generation and evolution of equatorial spread F. J Geophys Res Space Phys 104(A9):19859–19869. https://doi.org/10.1029/1999JA900271

Figueiredo CAOB, Takahashi H, Wrasse CM, Otsuka Y, Shiokawa K, Barros D (2018) Investigation of nighttime MSTIDS observed by optical thermosphere imagers at low latitudes: Morphology, propagation direction, and wind filtering. J Geophys Res Space Physics 123:7843–7857. https://doi.org/10.1029/2018JA025438

Haase JS, Dautermann T, Taylor MJ, Chapagain N, Calais E, Pautet D (2011) Propagation of plasma bubbles observed in Brazil from GPS and airglow data. Adv Space Res 47(10):1758–1776

Jiang C et al (2015) Simultaneous observations of F2 layer stratification and spread F at post-midnight over a northern equatorial anomaly region. J Geophys Res Space Physics 120:10979–10991. https://doi.org/10.1002/2015JA021861

Jiang C, Yang G, Liu J, Yokoyama T, Komolmis T, Song H, Lan T, Zhou C, Zhang Y, Zhao Z (2016) Ionosonde observations of daytime spread F at low latitudes. J Geophys Res Space Phys 121:12093–12103. https://doi.org/10.1002/2016JA023123

Kil H (2015) The morphology of equatorial plasma bubbles - a review. J Astron Space Sciences. https://doi.org/10.5140/jass.2015.32.1.13

Kil H (2022) The occurrence climatology of equatorial plasma bubbles: a review. J Astron Space Sci. https://doi.org/10.5140/JASS.2022.39.2.23

Liu H, Watanabe S, Kondo T (2009) Fast thermospheric wind jet at the Earth's dip equator. Geophys Res Lett. https://doi.org/10.1029/2009GL037377

Makela JJ, Kelley MC (2003) Field-aligned 7774-nm composite airglow images of equatorial plasma depletions. Geophys Res Lett. https://doi.org/10.1029/2009GL037377

Martinis C, Eccles JV, Baumgardner J, Manzano J, Mendillo M (2003) Latitude dependence of zonal plasma drifts obtained from dual-site airglow observations. J Geophys Res Space Phys. https://doi.org/10.1029/2002JA009462

Martinis C, Baumgardner J, Smith SM, Colerico M, Mendillo M (2006) Imaging science at El Leoncito Argentina. Ann Geophys. https://doi.org/10.5194/angeo-24-1375-2006

Martinis C, Baumgardner J, Wroten J, Mendillo M (2010) Seasonal dependence of MSTIDs obtained from 6300 nm airglow imaging at Arecibo. Geophys Res Lett. https://doi.org/10.1029/2010GL043569

Martinis C, Baumgardner J, Wroten J, Mendillo M (2018) All-sky-imaging capabilities for ionospheric space weather research using geomagnetic conjugate point observing sites. Adv Space Res. https://doi.org/10.1016/j.asr.2017.07.021

Meenakshi S, Sridharan S, Ivan JS (2022) Tidal influence on the longitudinal variabilities of the post-midnight spread F during September 2019. Adv Space Res 69(1):111–120

Panda D, Senapati B, Tyagi B, Kundu B (2019) Effects of Rayleigh-Taylor instability and ionospheric plasma bubbles on the global navigation satellite System signal. J Asian Earth Sci 170:225–233

Park J, Lühr H (2013) Relation of zonal plasma drift and wind in the equatorial F region as derived from CHAMP observations. Ann Geophys. https://doi.org/10.5194/angeo-31-1035-2013

Patil AS, Nade DP, Taori A, Pawar RP, Pawar SM, Nikte SS, Pawar SD (2023) A brief review of equatorial plasma bubbles. Space Sci Rev 219(1):16

Qiang LI, Yanbo ZHU, Zhipeng WANG, Kun FANG (2021) A method for automatic detection and characterization of plasma bubbles using GPS and BDS data. Chin J Aeronaut 34(5):195–204

Sejima H, Hosokawa K, Nakata H, Chum J, Lin CH, Lin JT (2023) Simultaneous observations of equatorial plasma bubbles with an all-sky airglow imager and a HF Doppler sounding system in Taiwan. Earth, Planets and Space 75(1):156

Sekar R, Chakrabarty D, Narayanan R, Patra AK (2008, December). Equatorial Spread F structures and associated airglow intensity variations observed over Gadanki. In Annales Geophysicae (Vol. 26, No. 12, pp. 3863–3873)

Shinbori A, Sori T, Otsuka Y, Nishioka M, Perwitasari S, Tsuda T, Shinohara I (2023) Generation of equatorial plasma bubble after the 2022 Tonga volcanic eruption. Sci Rep 13(1):6450

Takahashi H, Wrasse CM, Figueiredo CAOB, Barros D, Abdu MA, Otsuka Y, Shiokawa K (2018) Equatorial plasma bubble seeding by MSTIDs in the ionosphere. Prog Earth Planet Sci 5(1):1–13

Taori A, Parihar N, Ghodpage R, Dashora N, Sripathi S, Kherani EA, Patil PT (2015) Probing the possible trigger mechanisms of an equatorial plasma bubble event based on multi-station optical data. J Geophys Res Space Phys 120:8835–8847

Zalesak ST, Ossakow SL, Chaturvedi PK (1982) Nonlinear equatorial spread F: The effect of neutral winds and background Pedersen conductivity. J Geophys Res Space Phys 87(A1):151–166

Publisher's Note